Journal of X-Ray Science and Technology 21 (2013) 357–372
DOI 10.3233/XST-130384
IOS Press

Metal artifact reduction in CT by identifying missing data hidden in metals

Hyoung Suk Park[a], Jae Kyu Choi[a], Kyung-Ran Park[b], Kyung Sang Kim[c], Sang-Hwy Lee[b], Jong Chul Ye[c] and Jin Keun Seo[a,*]
[a]*Department of Computational Science and Engineering, Yonsei University, Seoul, Korea*
[b]*Department of Dentistry, Yonsei University, Seoul, Korea*
[c]*Bio-Imaging and Signal Processing Laboratory, Department of Bio and Brain Engineering, Korea Advanced Institute of Science and Technology, Daejon, Korea*

Received 17 August 2012
Revised 23 April 2013
Accepted 15 May 2013

Abstract. There is increasing demand in the field of dental and medical radiography for effective metal artifact reduction (MAR) in computed tomography (CT) because artifact caused by metallic objects causes serious image degradation that obscures information regarding the teeth and/or other biological structures. This paper presents a new MAR method that uses the Laplacian operator to reveal background projection data hidden in regions containing data from metal. In the proposed method, we attempted to decompose the projection data into two parts: data from metal only (metal data), and background data in the absence of metal. Removing metal data from the projections enables us to perform sparsity-driven reconstruction of the metal component and subsequent removal of the metal artifact. The results of clinical experiments demonstrated that the proposed MAR algorithm improves image quality and increases the standard of 3D reconstruction images of the teeth and mandible.

Keywords: Metal artifact reduction, dental X-ray CT, poisson equation, compressed sensing, sparsity

1. Introduction

In computerized tomography (CT), the presence of metallic objects such as gold crowns and implants causes streak artifact in the field of view [25]. The artifact appears as dark and bright streaks, and is caused by physical effects such as beam hardening, scattered radiation, nonlinear partial volume effect (NLPV), and noise [20]. This artifact can seriously damage the visibility and quality of the CT images, especially at the dental surface of metal restorations and their adjacent biological structures.

Metal artifact reduction (MAR) is an important development towards improving the quality of radiographs in the majority of dental and medical fields, including radiographic imaging, craniomaxillofacial and orthopedic surgery, oncology, and dental implants and prosthodontics. MAR is becoming increasingly crucial as demand increases for high-quality CT in diverse applications that include forensic dental identification [12] and rapid prototyping (RP) of dental and/or biological structures.

*Corresponding author: Jin Keun Seo, Department of Computational Science and Engineering, Yonsei University, 134 Sinchon-dong Seodaemun-gu, Seoul 120-749, Korea. E-mail: seoj@yonsei.ac.kr.

Since Lewitt and Bates [17] introduced the first MAR method in the late 1970s, various MAR methods have been suggested [2], most of which fall into one of the following three categories [21]: inpainting-based methods, iterative reconstruction methods, and hybrid methods that combine the first two methods. In inpainting-based methods, unreliable background data affected by the presence of metallic objects are recovered by various kinds of inpainting techniques such as linear interpolation (LI) [14,17,19], higher-order polynomial interpolation [1,5,23], wavelets [29,30], Fourier transform [15], tissue-class models [4], normalized interpolation methods [20], and total variation (TV) [8] or fractional-order inpainting methods [28]. However, numerous previous studies using inpainting-based methods have shown that inaccurate interpolation of the projection data introduces additional streaking artifacts in the reconstructed image [20,22]. In iterative reconstruction methods such as maximum-likelihood for transmission (ML-TR) [18], expectation maximization (EM) [24,26], iterative maximum-likelihood polychromatic algorithm for CT (IMPACT) [19], and metal shape reconstruction [27], the data fitting method is employed to reduce streaking artifact caused by the discrepancy between the projection data and the Radon transform of a function. However, its primary disadvantage is the high computational load [9], which means that for practical applications, development of the reconstruction process is reliant on advances in computational technology.

Unlike the existing methods that fill the region of data from metal (metal region) with synthesized data based on data from outside of the metal region, this paper presents a new method that decomposes the projection data into two parts using projection data that include the metal region: data from metal only (metal data) and background data in the absence of metal. The proposed method first restores the missing projection data masked by the influence of the metal. Based on the fact that the Laplacian of an image highlights abrupt changes in intensity, we applied the Laplacian operator to projection data to capture dental information hidden by data from metal. The background projection can be identified with the influence of metal data eliminated by solving a Poisson-type equation with Dirichlet boundary conditions in the region containing metal. The outlines of the teeth and bones are more accurate in the resultant images, which were made by highlighting data from the small amount of teeth and bone data in metal region. In the next step, we focused on treatment of the metal part. Taking advantage of the sparseness of metallic objects, we can exploit the compressed sensing (CS) theory [7,10], which guarantees the accurate reconstruction of metals and significantly reduces the total computational burden of the iterative process. We then empirically evaluated the efficacy of the algorithm by comparing 3D dental images reconstructed from a set of projection data, with and without the algorithm.

2. Methods

2.1. Metal artifact

We briefly review the beam hardening effect as the major cause of metal artifact. This artifact can be explained in terms of the relation between the CT image and the X-ray data. Let $f_E(\mathbf{r})$ be the attenuation coefficient at point $\mathbf{r} = (x, y, z)$ and energy level E, and let $I^0(E)$ be the intensity of the incident X-ray beam at energy level E. Let P_θ denote the two-dimensional image representing X-ray projection data along direction $\Theta = (\cos\theta, \sin\theta, 0)$. For ease of explanation, let us consider the case of a two-dimensional parallel CT beam with setting z as a fixed constant z_0. Then, the CT-image f_{CT} reconstructed by the widely used filtered back-projection algorithm can be related to the X-ray data (or projection data), denoted by P_θ, in the following way [6]:

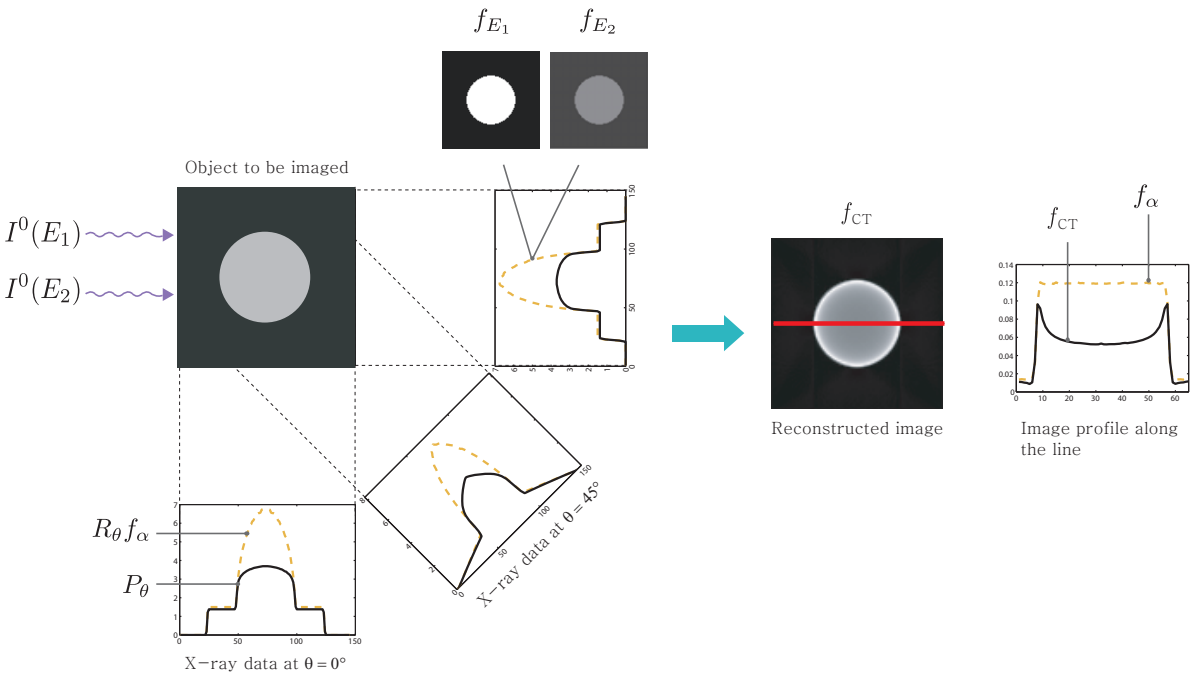

Fig. 1. Illustration of the nonlinear effect. (Colours are visible in the online version of the article; http://dx.doi.org/10.3233/XST-130384)

$$\text{(X-ray data) } P_\theta(s,z_0) = -\ln\left(\int_{E_{\min}}^{E_{\max}} I^0(E)\exp\{-\mathcal{R}_\theta f_E(s,z_0)\}dE\right) + \ln I^0$$

$$\text{(CT image) } f_{CT}(\mathbf{r}) = \int_0^\pi (P_\theta * \mathcal{F}^{-1}\{|k|\})(\mathbf{r}\cdot\Theta)d\theta \tag{1}$$

where $\mathcal{R}_\theta f_E(s,z) := \int\int f_E(\mathbf{r})\delta(\mathbf{r}\cdot\Theta - s)dxdy$ denotes the Radon transform of f_E along the direction $\Theta = (\cos\theta, \sin\theta, 0)$, $\mathcal{F}^{-1}$ is the inverse Fourier transform, and $I^0 = \int_{E_{\min}}^{E_{\max}} I^0(E)dE$ is the total intensity of the incident X-ray beam.

The presence of metal produces severe beam hardening artifact in CT images because the X-ray beam has multiple energy levels and the attenuation coefficients of metals have much stronger nonlinearity with respect to the energy level E than do tooth and tissue. As an example, consider the special case when the X-ray beam is bi-chromatic having two dominant energy levels E_1 and E_2, with $E_1 < E_2$. Assume that f_{E_1} and f_{E_2} are

$$f_{E_1}(\mathbf{r}) = \begin{cases} 0.2 & \mathbf{r}\in D \\ 0.01 & \text{otherwise} \end{cases}, \quad f_{E_2}(\mathbf{r}) = \begin{cases} 0.04 & \mathbf{r}\in D \\ 0.02 & \text{otherwise} \end{cases}$$

and their images are shown in Fig. 1. However, the reconstructed CT-image f_{CT} is not constant in a disk D, while the object in D is homogeneous. Figure 1 illustrates this phenomenon at a cross sectional view.

Figure 2 shows streaking artifact caused by the presence of metal. The major cause of this artifact is metal because the attenuation coefficients of metals vary greatly with respect to the energy level E, whereas those of bone and tissue do not.

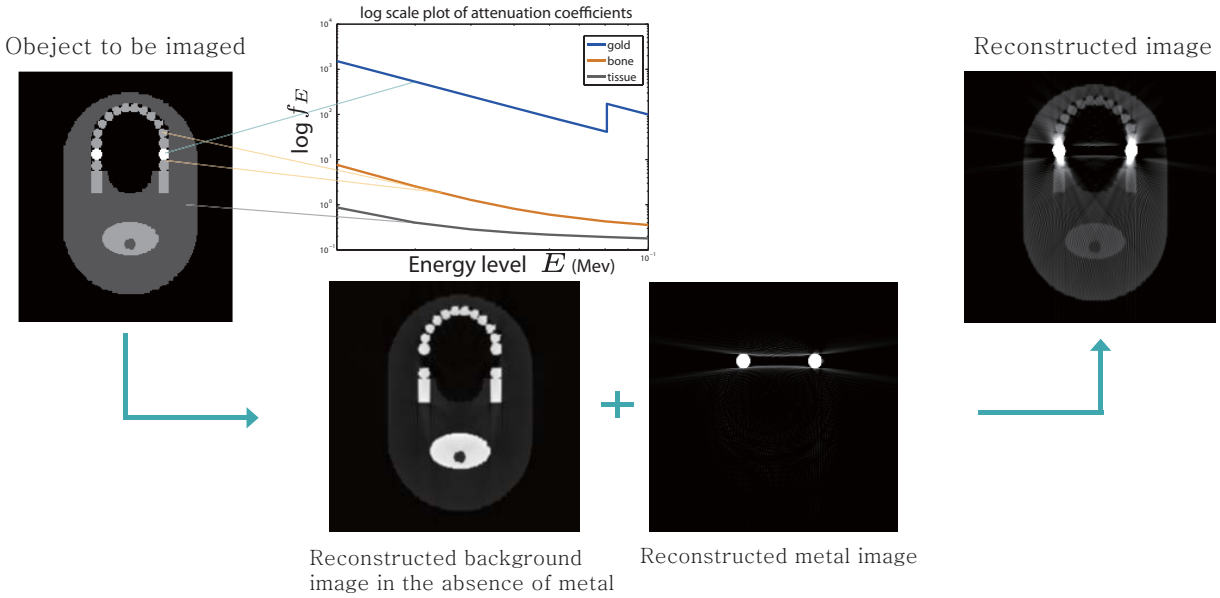

Fig. 2. Jaw phantom image showing streaking artifact. (Colours are visible in the online version of the article; http://dx.doi.org/10.3233/XST-130384)

Fig. 3. Phantom experiment: (a) Teeth phantom containing metal. Decomposition of X-ray data (b) $P_\theta(\mathbf{x})$ into (c) $u_\theta(\mathbf{x})$ and (d) $w_\theta(\mathbf{x})$, generated at 70 keV and 15 mA, shown with a display window [0 4000]. (Colours are visible in the online version of the article; http://dx.doi.org/10.3233/XST-130384)

2.2. Method for metal removal and background reconstruction

2.2.1. Decomposition of the projections

With a fixed angle θ of projection, let us focus on $P_\theta(\mathbf{x})$ with $\mathbf{x} = (s, z)$ in Section 2.1. To deal with the metal artifact, we attempted to decompose the projection data P_θ into two parts:

$$P_\theta(\mathbf{x}) = u_\theta(\mathbf{x}) + w_\theta(\mathbf{x}), \tag{2}$$

where $w_\theta(\mathbf{x})$ is the projection data from metal only, and $u_\theta(\mathbf{x})$ is the background projection in the absence of metal. Figure 3 illustrates the decomposition of Eq. (2) with minor decomposition error. Note that $u_\theta(\mathbf{x})$ shows a reasonably linear relationship with the corresponding CT image, so that the filtered back-projection algorithm in Eq. (1) provides a sufficiently useful CT image. In contrast, $w_\theta(\mathbf{x})$ has strong nonlinearities, as mentioned in the previous Section 2.1. We can take advantage of prior information regarding metal in the CT image that should be constant in the domain containing metal (metal domain). This information is used to correct $w_\theta(\mathbf{x})$, to reduce the discrepancy between the Radon

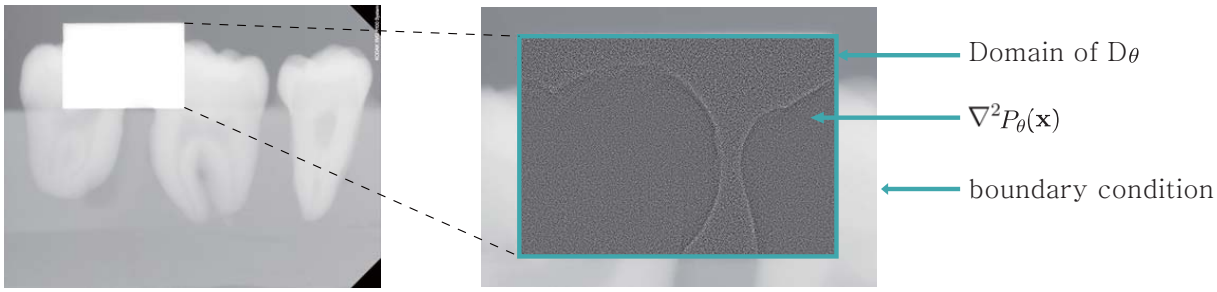

Fig. 4. Illustration of a Poisson problem with the boundary condition as in Eq. (5). The Laplacian of P_θ^{int} highlights the boundary information of teeth data hidden by metal data. (Colours are visible in the online version of the article; http://dx.doi.org/10.3233/XST-130384)

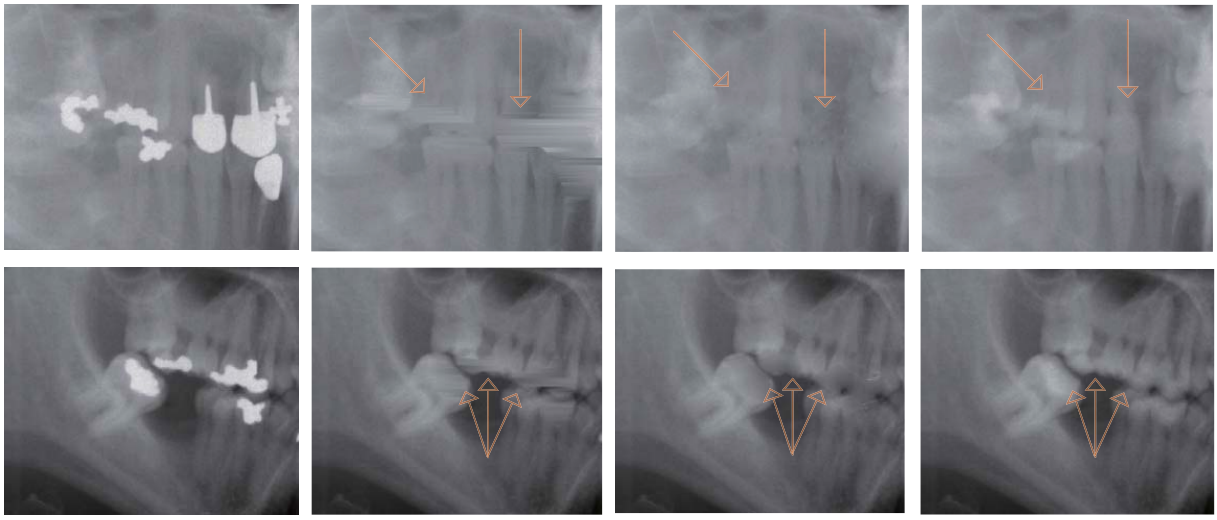

Fig. 5. The first column shows real projection data. The second, third, and fourth columns represent background data using LI, TV inpainting, and the proposed method, respectively. All the projection data and the reconstructed images are shown at a fixed gray scale level to enable fair comparison. (Colours are visible in the online version of the article; http://dx.doi.org/10.3233/XST-130384)

transform of the metal image and its projection data $w_\theta(\mathbf{x})$. This is the main reason why decomposition of Eq. (2) is important in MAR.

Assume that the three-dimensional domain D occupies the metal domain. Let D_θ be a forward projection on D with angle θ. In the decomposition (2), we first extract the metal region D_θ using the projection data P_θ and the uncorrected image f_{CT}. By performing a simple thresholding on the uncorrected CT image f_{CT} in (1), we determine an approximate metal domain $\tilde{D}$ that is reasonably close to D. By combining the simple thresholding on $\nabla^2 P_\theta(\mathbf{x})$ and the forward projection $\tilde{D}_\theta$ of $\tilde{D}$, we can determine D_θ much more accurately. For convenience, we denote

$$P_\theta(\mathbf{x}) = \begin{cases} P_\theta^{ext}(\mathbf{x}) \text{ if } \mathbf{x} \notin D_\theta \\ P_\theta^{int}(\mathbf{x}) \text{ if } \mathbf{x} \in D_\theta, \end{cases} \tag{3}$$

and we use the same notation for $u_\theta(\mathbf{x})$ and $w_\theta(\mathbf{x})$.

The key idea that underlies the reconstruction of $u_\theta^{int}(\mathbf{x})$ in D_θ is that $\nabla^2 P_\theta^{int}(\mathbf{x})$ may reveal the boundary of a tooth that is obscured by metal data, as shown in Fig. 4. We can then compute $u_\theta^{int}(\mathbf{x})$ in

D_θ by solving the following Poisson equation with Dirichlet boundary conditions:

$$\begin{cases} \nabla^2 u_\theta^{int} = \eta(\nabla^2 P_\theta^{int}) \text{ in } D_\theta \\ u_\theta^{int} = P_\theta^{ext} \text{ on } \partial D_\theta, \end{cases} \tag{4}$$

where η is an operator suitably chosen to keep the boundary information of teeth and bone data in D_θ while eliminating the influence of metal data. If the operator η is chosen to be the identity map, then u_θ in Eq. (4) becomes the solution to

$$\begin{cases} \nabla^2 u_\theta^{int} = \nabla^2 P_\theta^{int} \text{ in } D_\theta \\ u_\theta^{int} = P_\theta^{ext} \text{ on } \partial D_\theta, \end{cases} \tag{5}$$

and w_θ is the solution to

$$\begin{cases} \nabla^2 w_\theta^{int} = 0 \text{ in } D_\theta \\ w_\theta^{int} = P_\theta^{int} - u_\theta^{int} \text{ on } \partial D_\theta. \end{cases} \tag{6}$$

Using the solution to Eq. (5), the global u_θ can be expressed as

$$u_\theta(\mathbf{x}) = P_\theta^{ext}(\mathbf{x})(1 - \chi_{D_\theta}(\mathbf{x})) + u_\theta^{int}(\mathbf{x})\chi_{D_\theta}(\mathbf{x}) \tag{7}$$

where χ_{D_θ} is the indicator function of the region D_θ, which takes a value of one in D_θ and zero otherwise. Having obtained u_θ for all angles θ, we can reconstruct the background image with acceptable accuracy via the conventional reconstruction algorithm. Numerically, we solve Eq. (4) using the finite difference method (FDM) [3]. Figure 5 shows the comparison among LI [17], TV-inpainting [11], and our proposed decomposition method in a clinical projection data.

2.2.2. Sparsity-based reconstruction of metal component

Finally, we carry out the metallic object reconstruction based on the data w_θ and the domain $\tilde{D}$ as a good initial guess (obtained by thresholding). In particular, we consider the metal component of the reconstruction problem under the sparsity constraint: find D that minimizes its volume $|D|$ subject to the constraint

$$\int_0^{2\pi} \left(\iint |w_\theta - \mathcal{R}_\theta(f^0 \chi_D)|^2 m_\theta d\mathbf{x} \right) d\theta < \epsilon, \tag{8}$$

where $f^0(\mathbf{r})$ represents the distribution of the attenuation coefficients of the metal, and $m_\theta(\mathbf{x})$ denotes the number of measured X-ray photons at position $\mathbf{x}$.

For the numerical implementation, we will use the sparsity-based method for reconstruction of metal components, as described in [9]. For clarity, the procedure is briefly described here. Let l_{ij} be the effective intersection length of projection line i with voxel j. Define $\mathbf{p} = [p_1\, p_2 \cdots p_M]^T$, $\mathbf{u} = [u_1\, u_2 \cdots u_M]^T$, $\mathbf{w} = [w_1\, w_2 \cdots w_M]^T$, and $\mathbf{L} = [l_{ij}]$, where $1 \leqslant i \leqslant N$ and $1 \leqslant j \leqslant M$, as the discretizations of P_θ, u_θ, w_θ, and $\mathcal{R}_\theta$, respectively. Let $\mathbf{f} = [f_1\, f_2 \cdots f_N]^T$ be an unknown attenuation coefficient to be determined. Under the assumption of a monochromatic incident X-ray beam with a constant I^0, the expected number of measured X-ray photons $\mathbf{y}$ is represented as:

$$y_i = I^0 \exp\left(-\sum_{j=1}^{M} l_{ij} f_j \right), \quad 1 \leqslant i \leqslant M. \tag{9}$$

Let $\tilde{\mathbf{y}} = [\tilde{y_1}\, \tilde{y_2} \cdots \tilde{y_M}]^T$ be the measured number of X-ray photons. Because $\tilde{y_i}$'s are mutually independent, the probability of measuring $\tilde{y_i}$ depends only on its expected value y_i, and the photon counts

follow the Poisson distribution; consequently, we obtain the log-likelihood function:

$$L(\mathbf{f}) = \sum_{i=1}^{M} \ln P(\tilde{y_i}|\mathbf{f}) = \sum_{i=1}^{M} \ln P(\tilde{y_i}|y_i) = \sum_{i=1}^{M} (\tilde{y_i} \ln y_i - y_i - \ln \tilde{y_i}!). \tag{10}$$

From Eq. (9), we can determine the expected value of projection data p_i and the actual measurement $\tilde{p_i}$:

$$p_i = -\ln \frac{y_i}{I^0} = \sum_{j=1}^{N} l_{ij} f_j, \quad \tilde{p_i} = -\ln \frac{\tilde{y_i}}{I^0}. \tag{11}$$

Using the background projection data $\mathbf{u}$ obtained from our proposed method, we can then obtain the estimated background image $\tilde{\mathbf{f}}^b = [\tilde{f_1}^b \ \tilde{f_2}^b \cdots \tilde{f_N}^b]^T$ using the approximated filtered back-projection, termed the Feldkamp (FDK) algorithm [13]. Therefore, $\mathbf{f}$ can be decomposed into $\tilde{\mathbf{f}}^b$ and the residual image $\Delta\mathbf{f}$ can be expected to consist mainly of metal, which leads to the following:

$$\tilde{w_i} = \tilde{p_i} - u_i = -\ln \frac{\tilde{y_i}}{I^0} - u_i, \tag{12}$$

$$w_i = p_i - u_i = -\ln \frac{y_i}{I^0} - u_i = \sum_{j=1}^{N} l_{ij} \Delta f_j, \quad i = 1, \cdots, M. \tag{13}$$

Using the above quantities, the log-likelihood function (10) can be approximated as a quadratic function of $\Delta\mathbf{f}$:

$$L(\Delta\mathbf{f}) \approx -\frac{1}{2} \|\tilde{\mathbf{w}} - \mathbf{L}\Delta\mathbf{f}\|^2_{\mathbf{M}} + \text{constant}, \tag{14}$$

where $\mathbf{M}$ denotes the diagonal matrix $\mathbf{M} = diag(\tilde{y_i})$. To overcome the inconsistency, we adopt the following metal component reconstruction problem under the sparsity constraint as in [9]:

$$\min \ \|\Delta\mathbf{f}\|_1 \quad \text{subject to} \quad \|\tilde{\mathbf{w}} - \mathbf{L}\Delta\mathbf{f}\|^2_{\mathbf{M}} < \epsilon. \tag{15}$$

2.2.3. Procedures for the proposed MAR algorithm

Unlike the conventional inpainting applications, the new method of metal artifact reduction presented here is based on Poisson's equation. Briefly, the proposed method is based on the following steps:

1. Given a set of projection data containing the data from metal, reconstruct the uncorrected 3D image using the FDK algorithm.
2. Using a simple thresholding, find the metallic object image in the reconstructed image.
3. Find the metal regions in the projection data using forward projection of the metallic object image.
4. Extract the background data in the metal regions by solving Poisson's equation locally.
5. Reconstruct the global 3D background image with these background data.
6. The corrected metallic object image that is obtained from the residual data, based on the sparsity of the metal image, is added to the 3D background image.

In short, the proposed method can be described as in Fig. 6.

3. Experimental results

3.1. Phantom experiment

For the phantom X-ray data shown in Fig. 3, we performed error estimation based on the normalized absolute difference (NAD). All errors computed from the absolute difference with the reference data

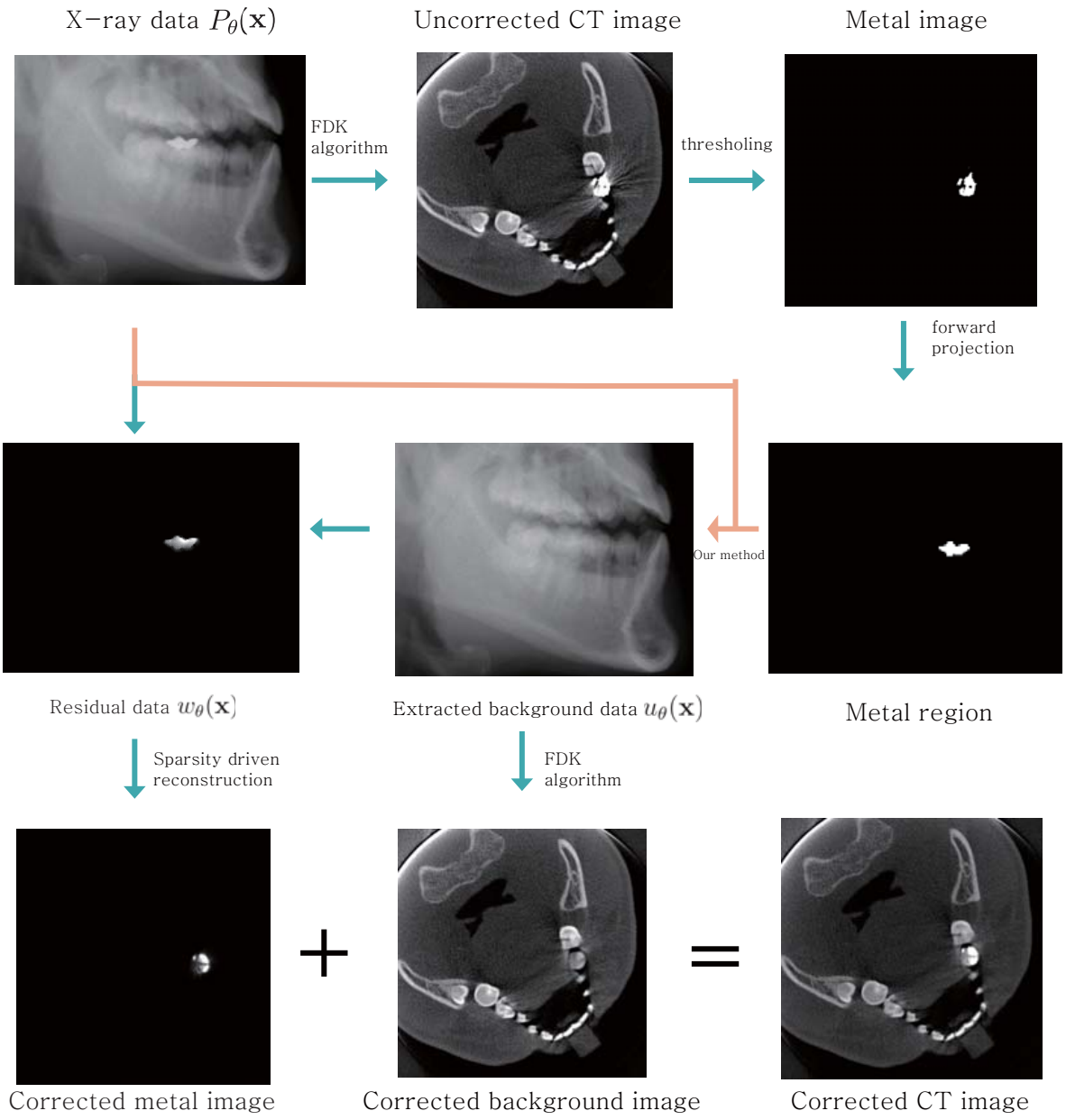

Fig. 6. Summary diagram of the MAR method. (Colours are visible in the online version of the article; http://dx.doi.org/10.3233/XST-130384)

were normalized using the X-ray data error of the data from metal [16]. As shown in Fig. 7, the NAD of the proposed method is 8.5%, which is less than the 27.5% of TV inpainting. In this case, the proposed method works better than the TV inpainting method for recovering the morphology of teeth data hidden by metal data because TV inpainting may produce an inaccurate image due to the nature of total variation minimization.

The efficacy of the proposed method for improving the reconstructed image was tested using the jaw

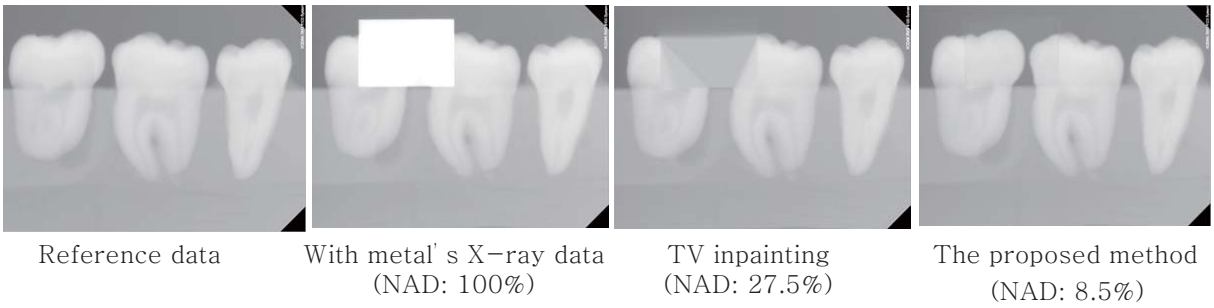

Fig. 7. Comparison of errors (NAD) between TV inpainting and the proposed method.

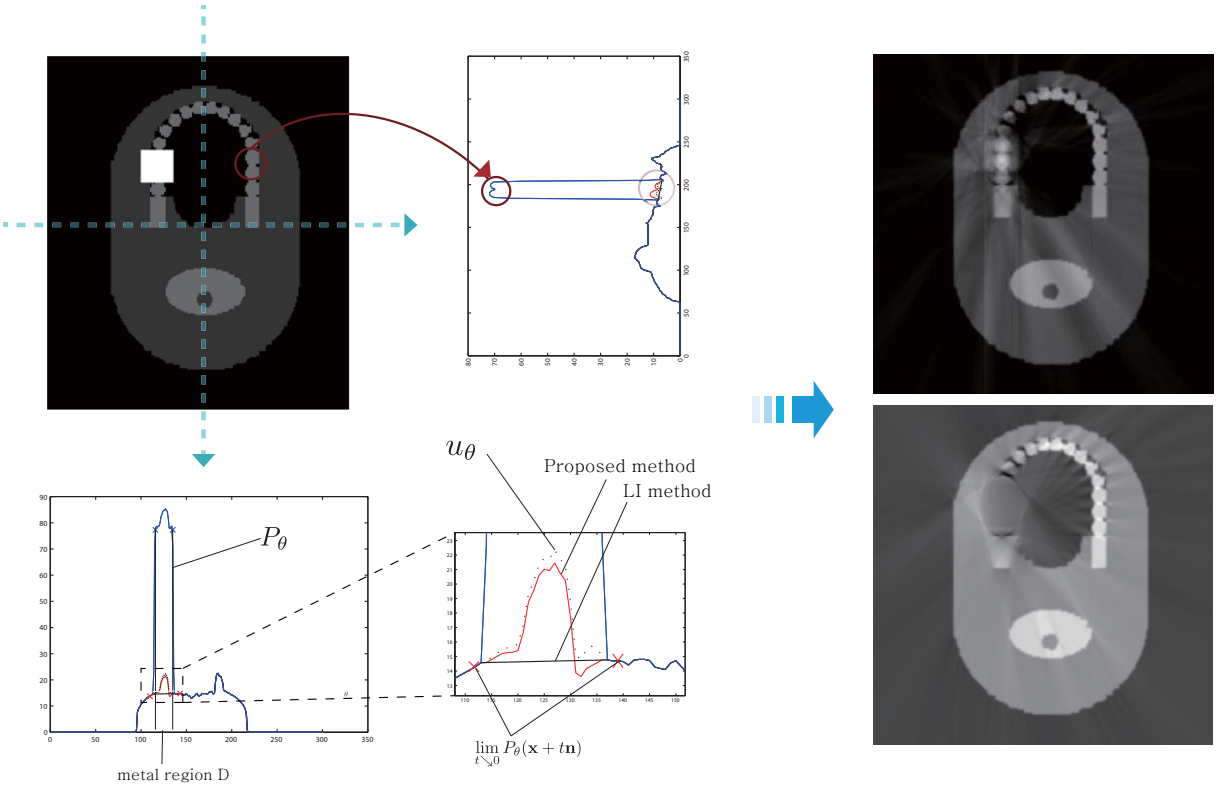

Fig. 8. Comparison between LI and the proposed method. (Colours are visible in the online version of the article; http://dx.doi.org/10.3233/XST-130384)

phantom developed by [Oliver Watzke] (See Fig. 8). A square metallic object is seen covering two teeth. Projection data of the jaw phantom at $\theta = 0°$ and $90°$ are shown. The red line denotes the corrected projection data obtained by the proposed method, and the resultant reconstructed image is shown in the upper right corner. Only the metallic object is removed, revealing teeth previously obscured by metal. The projection data using LI show the metal region as a black line, and the resulting reconstruction image is shown in the bottom right corner. Teeth information near the metallic object is completely removed because the teeth projection data near the metal region are removed over the whole angle by linear interpolation.

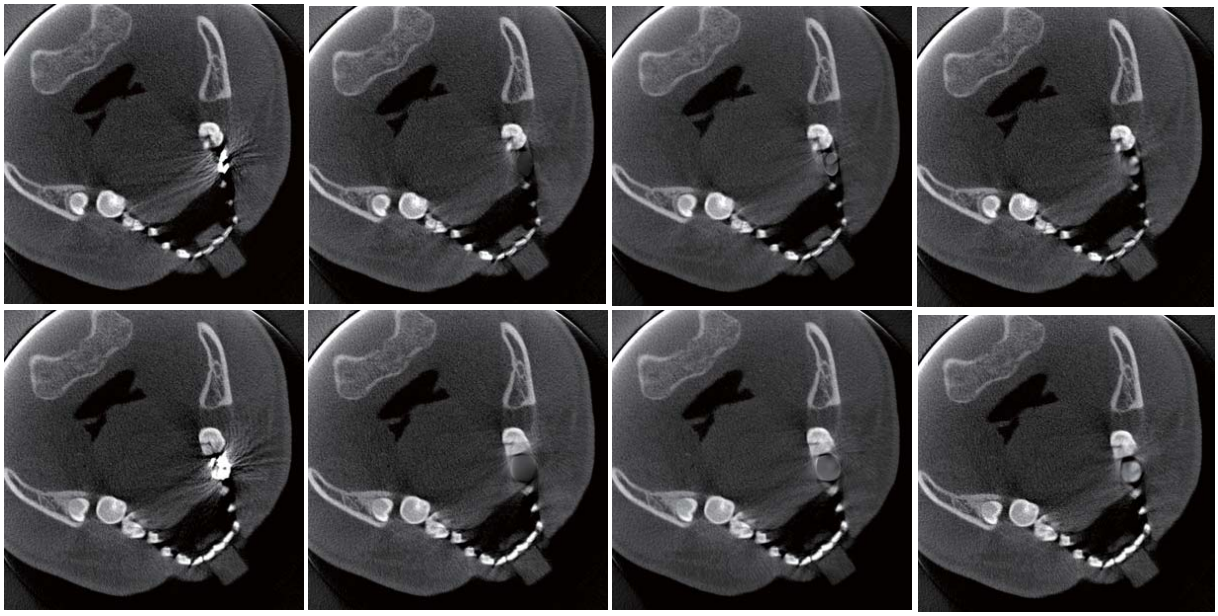

Fig. 9. First row: Left image shows a slice image of a reconstructed 3-dimensional jaw. The second, third, and fourth images show corrected slice images from the corrected background data using LI, TV-inpainting, and the proposed method, respectively. Second row shows results for a second slice image position.

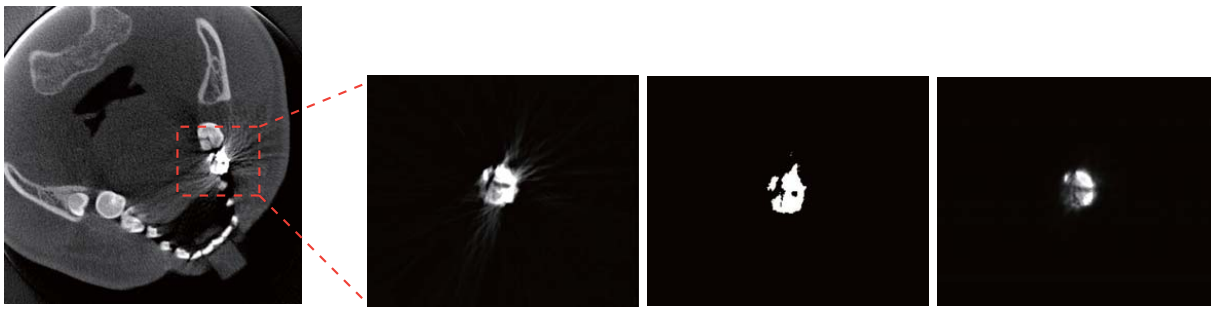

Fig. 10. Results of metal reconstruction: comparison among the FDK algorithm (second image), simple thresholding (third image), and sparsity-driven MAR method (fourth image). (Colours are visible in the online version of the article; http://dx.doi.org/10.3233/XST-130384)

3.2. Patient measurements

To verify the effectiveness of the proposed method, we performed experiments using a flat-detector conebeam CT, RAYSCAN Symphony V (Ray Co., Suwon, South Korea), which generates a tube voltage of 60–90 kVp. Images were obtained using 600 projection data sets with a field of view (FOV) of 15 cm $\times$ 7 cm and a 768 $\times$ 960-pixel detector (pixel size of 0.254 mm).

A comparison among LI, TV-inpainting, and the proposed method is shown in Fig. 9. The first column shows slice CT images obtained with FDK reconstruction algorithm at two different cross-sections. The second and third columns show slice CT images corrected using LI and TV-inpainting at two different cross-sections, while the fourth column depicts slice CT images corrected using the proposed method at

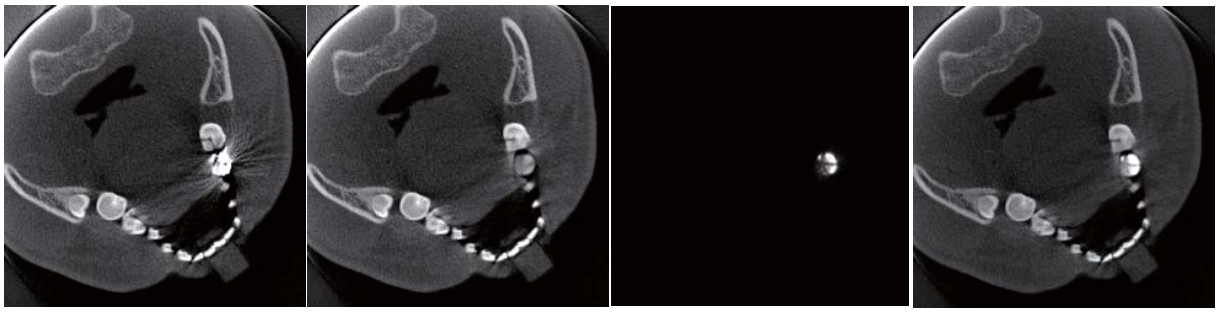

Fig. 11. Comparison between the original reconstructed image (far left) and the final corrected image (far right).

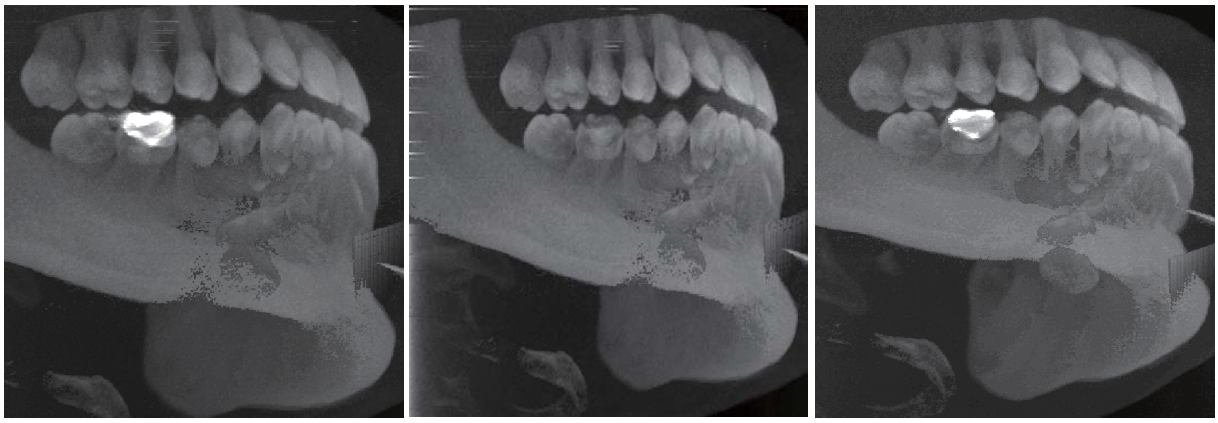

Fig. 12. Three-dimensional reconstructed images: original CT reconstruction (left), background reconstruction (center), and final corrected CT reconstruction (right).

two different cross-sections. All three of the methods reduce the streaking artifact around the metallic object; however, the reconstructed CT image using LI loses background information around the metal domain. The reconstructed image using TV-inpainting can recover background information in the metal domain, but it is also inaccurate. In contrast, new streaking artifact is less severe with the proposed method than with LI and TV-inpainting, and this method also preserves background information near metal domain.

Figure 10 shows the results for reconstruction of a metal image using FDK (second image), simple thresholding (third image), and the sparsity-driven MAR method (fourth image). Because it is difficult to determine an optimal thresholding value, we cannot obtain a robust metal image; this is apparent on the second image. However, the sparsity of the metal image enabled us to obtain a stably corrected metal image (fourth image) even though we used 20 uniformly sampled X-ray data out of 600, as described in [9].

Figure 11 compares the original reconstructed image with the final corrected image. The first image on the left shows an original slice CT image taken with FDK reconstruction algorithm, the second subfigure is a corrected background image using the proposed method, the third is a corrected metal image using the sparsity-based minimization method, and the fourth is the final corrected image obtained by adding the corrected metal image to the corrected background image. The fourth image of Fig. 11 shows a reduction in streaking artifact as well as recovery of morphological information from teeth that are covered with metal. The effectiveness of the proposed method for reducing streaking artifact is also

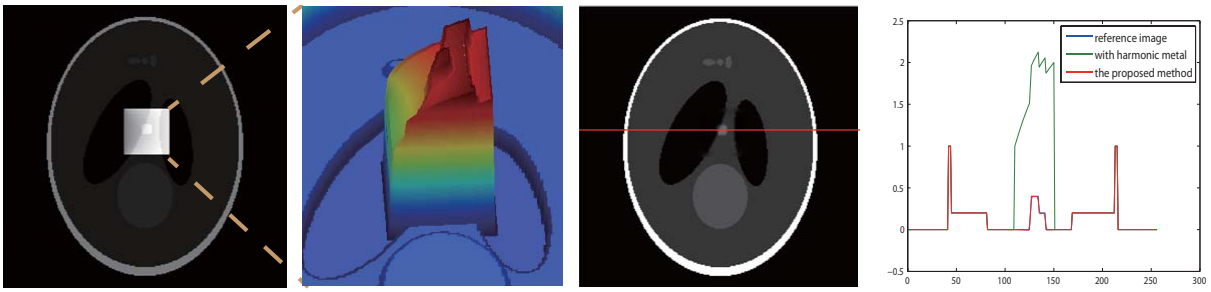

Fig. 13. Efficacy of the proposed method with a nonuniform but harmonic metal region. (Colours are visible in the online version of the article; http://dx.doi.org/10.3233/XST-130384)

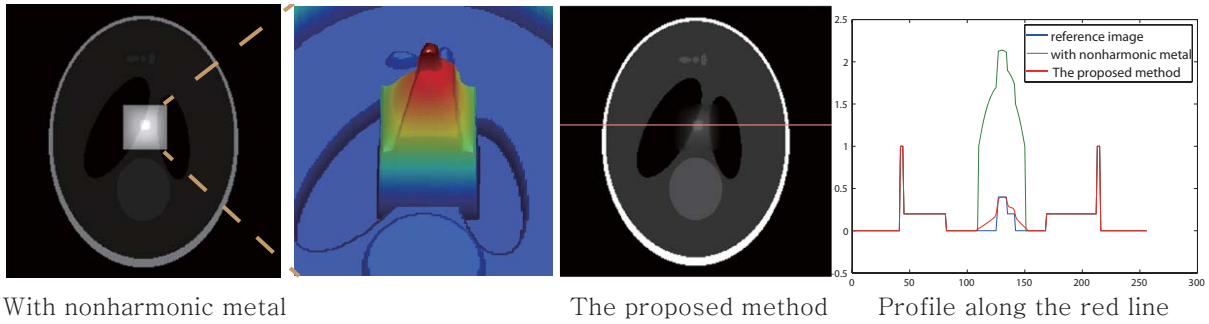

Fig. 14. Efficacy of the proposed method with a nonuniform and nonharmonic metal region. (Colours are visible in the online version of the article; http://dx.doi.org/10.3233/XST-130384)

verified on the three-dimensional view, as shown in the third subfigure of Fig. 12.

4. Discussion

The present results show that the projection data decomposition method based on the Poisson equation can extract background data by excluding X-ray data from metal. The reconstructed image demonstrates recovery of the morphology of teeth near the metallic object, and streaking artifact is reduced. As shown in Fig. 8, incorrect removal of metal X-ray data by LI creates new streaking artifact in the reconstructed CT image, for the reason that background data near the approximated metal region obtained by simple thresholding in the reconstructed image is interpolated along the rotational direction. Moreover, in this method, metal data and background data are removed from the region at the same time. Consequently, the effect of LI on the projection data is a loss of information in the reconstructed image, both for teeth surrounded by metal and for teeth near metal. The TV-inpainting method provides a better reconstructed image than LI, as shown in Fig. 9. However, it cannot effectively recover curved tooth-like outlines from the region surrounding the metal data because it always prefer the shortest connection as shown in Fig. 7. For this reason, the reconstructed image is still missing information for teeth surrounded by metal.

The proposed method uses Laplacian information to remove X-ray data from metal in the same approximated region. It is worth noting that the Laplacian of the X-ray data enables visualization of dental shape data that are obscured by metal data, as described in Fig. 4. Moreover, we can use the Laplacian information to determine the exact boundaries of metal in the approximate metal region. As mentioned

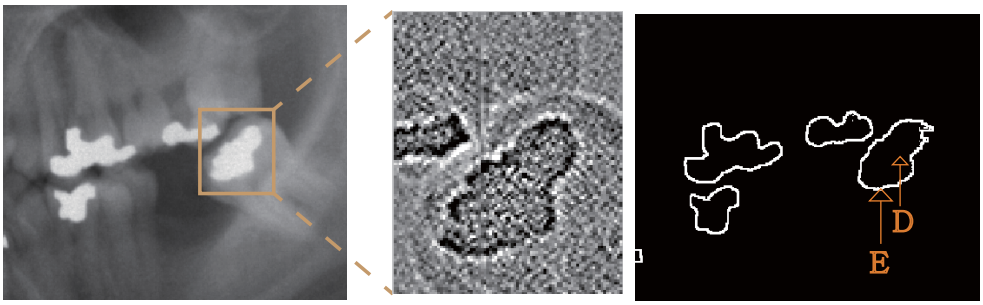

Fig. 15. Geometry of projection data containing data from metal. (Colours are visible in the online version of the article; http://dx.doi.org/10.3233/XST-130384)

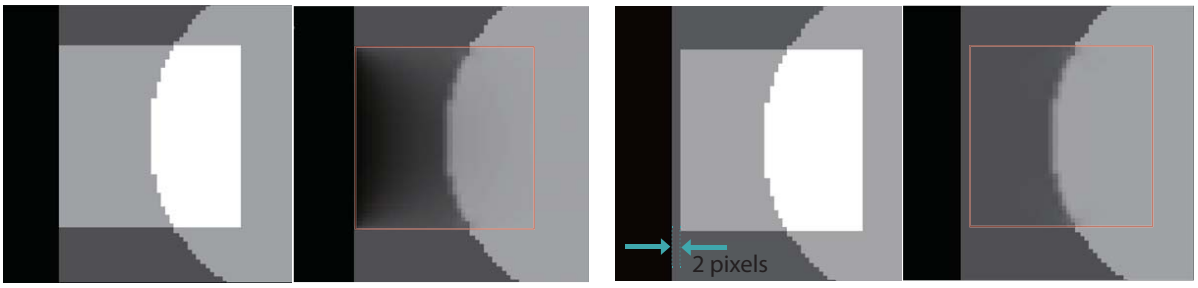

Fig. 16. Indistinguishable boundary caused by a common boundary shared by the projection of teeth and metal. In this special case, the proposed method fails to reconstruct the expected image because the boundary data are inaccurate. (Colours are visible in the online version of the article; http://dx.doi.org/10.3233/XST-130384)

previously, solving the proposed PDE equation with this appropriate boundary information enables us to remove X-ray data originating from metal from the measured X-ray data, while preserving data near the metal region and revealing background data obscured by data from metal (see Fig. 5). Compared with LI and TV-inpainting, the proposed method more effectively reduces streaking artifacts in the reconstructed image and preserves teeth information near the metallic object, as shown in Fig. 9. In addition, new artifacts introduced into the correction result are less severe with the proposed method than with LI and TV-inpainting. For these reasons, the proposed method is more advantageous than the LI and TV-inpainting methods in terms of reconstructing the background image, as verified by the present results.

Figure 10 shows that the quality of the reconstructed metal image can be improved. Adoption of the sparsity-driven minimization problem for reconstruction of metal image enables us to obtain more exact morphological and positional information of metal objects than the use of a simple thresholding method which can still retain streaking artifact around metal objects.

In the field of dentistry, the proposed method could become the method of choice for revealing background projection data, using the Laplacian operator to capture the geometry of teeth and bone data hidden by metal data. However, the proposed method has limited application in the case of patients with very thick metal (or for numerous metal objects). Thus, the method requires improvement to become suitable for wider applications. In the remainder of this section, we will present some limitations of the proposed method.

First, when the data from metal is of nonuniform thickness in the metal region, Eq. (4) should be used with care. For example, if there is no abrupt change in the thickness of the metal data, as in Fig. 13, then the Laplacian of the projection data effectively delineates the shape of background data hidden by metal data. In particular, when the Laplacian of metal data is negligible, the background data can be recovered accurately. However, in the case of an abrupt change in the thickness of metal data, as shown in Fig. 14, it becomes more difficult to extract the boundaries of background data from the metal region. Second, for multiple metallic objects, it is necessary to distinguish the Laplacian of teeth and metallic objects in the metal region, which is why we introduced the operator η in the present study. Our focus in future development of the proposed method is the appropriate choice of η according to the metal geometry. Furthermore, in the case where metal attenuates the X-ray beam so strongly that no photon reaches the detectors (photon starvation effect), the proposed method becomes the harmonic-inpainting method. To be more specific, in the case of photon starvation effect, we have $\nabla^2 u_\theta \approx 0$ and thus, Eq. (4) can be viewed as

$$u_\theta^{int} = \arg\min \int_{D_\theta} |\nabla u_\theta|^2 d\mathbf{x} \quad \text{subject to} \quad \int_{E_\theta} |u_\theta - P_\theta^{ext}|^2 d\mathbf{x} \leqslant \epsilon^2.$$

where D_θ denotes the metal region and E_θ is the extended region surrounding the boundary of D_θ (See Fig. 15). This case can have similarities with the TV inpainting method [8] by replacing the L2 norm of ∇u_θ with L1, because the Euler–Lagrange equation for this problem is

$$(1-\lambda_E)\nabla^2 u_\theta + \lambda_E(u_\theta - P_\theta^{int}) = 0, \quad \lambda_E = \begin{cases} \lambda & \mathbf{x} \in E_\theta \\ 0 & \mathbf{x} \in D_\theta \end{cases}$$

where λ is a Lagrange multiplier. Third, in the case of an indistinguishable boundary caused by a common boundary shared by the projection of teeth and metal, the proposed method fails to reconstruct the expected image because the boundary data are inaccurate. See Fig. 16. Further research is necessary to overcome these technical obstacles before the proposed method can be applied clinically.

5. Conclusions

We proposed a new MAR method that enables visualization of background projection data hidden in regions containing data from metal. We demonstrated numerically and experimentally that the proposed MAR algorithm improves image quality. The proposed technique utilizes Poisson equation to decompose the projection data into two parts: data from metal only and background data in the absence of metal. It is interesting that the Laplacian of the projection highlights the boundaries of teeth and bone data hidden by data from metal. Its ability to efficiently remove streaking from metal suggests its usefulness in diagnosis, preoperative and presurgical assessment, surgical navigation, and in workup for rapid prototyping.

The proposed method has limitations when the metal is very thick and when there are numerous metal objects. Future studies should focus on overcoming these technical barriers to develop the capability of the method for capturing more accurate outlines of teeth and bones.

Acknowledgements

HS Park, JK Choi and JK Seo were supported by the National Research Foundation of Korea (NRF), a grant funded by the Korean Government (MEST, No.2011-0028868(2012R1A2A1A03670512)) through the NRF funded by the Ministry of Education, Science and Technology.

References

[1] M. Abdoli, M. Ay, A. Ahmadian, R. Dierckx and H. Zaidi, Reduction of dental filling metallic artefacts in CT-based attenuation correction of PET data using weighted virtual sinograms optimized by a genetic algorithm, *Med Phys* **37** (2010), 6166–6177.

[2] M. Abdoli and H. Zabibi, Metal Artifact Reduction Strategies for Improved Attenuation Correction in Hybrid PET/CT Imaging, *Med Phys* **39** (2012), 3343–3360.

[3] K.E. Atkinson, An introduction to numerical analysis, John Wiley and Sons, New York-Chichester-Brisbane, ISBN: 0-471-02985-8, 65-01, 1978.

[4] M. Bal and L. Spies, Metal artifact reduction in CT using tissue-class modeling and adaptive prefiltering, *Med Phys* **33** (2006), 2852–2859.

[5] M. Bazalova, L. Beaulieu, S. Palefsky and F. Verhaegen, Correction of CT artifacts and its influence on Monte Carlo dose calculations, *Med Phys* **34** (2007), 2119–2132.

[6] R.N. Bracewell and A.C. Riddle, Inversion of fan-beam scans in radion astronomy, *Astrophys J* **150** (1967), 427–434.

[7] E. Candes, J. Romberg and T. Tao, Robust Uncertainty Principles: Exact Signal Recovery from Highly Incomplete Frequency Information, *IEEE Trans. on Information Theory* **52** (2006), 489–509.

[8] T.F. Chan and J. Shen, Mathematical Models for Local Non Texture Inpainting, *SIAM J Appl Math* **62** (2002), 1019–1043.

[9] J. Choi et al., Sparsity Driven Metal Part Reconstruction for Artifact Removal in Dental CT, *Journal of X-ray Science and Technology* **19** (2011), 457–475.

[10] D. Donoho, Compressed Sensing, *IEEE Trans. on Information Theory* **52** (2006), 1289–1306.

[11] X. Duan, L. Zhang, Y. Xiao, J. Cheng, Z. Chen and Y. Xing, Metal artifact reduction in CT images by sinogram TV inpainting, *IEEE Nuclear Science Symposium and Medical Imaging Conference* (19–25 Oct. 2008), 4175–4177.

[12] S.J. Esses et al., Clinical Applications of Physical 3D Models Derived from MDCT data and Created by Rapid Prototying, *AJR June* **196**(6) (2011), W683–W688.

[13] L.A. Feldkamp, L.C. Davis and J.W. Kress, Practical cone-beam algorithm, *J Opt Soc Am A* **1** (1984), 612–619.

[14] W. Kalender, R. Hebele and J. Ebersberger, Reduction of CT artifacts caused by metallic implants, *Radiol* **164** (1987), 576–577.

[15] B. Kratz, T. Knopp, J. Müller, M. Oehler and T.M. Buzug, Non-equispaced Fourier Transform vs. Polynomial Based Metal Artifact Reduction in Computed Tomography, Bildverarbeitung fuŕ die Medizin, Springer, Berlin, 2008, pp. 21–25.

[16] B. Kratz, S. Ens, J. Müller and T.M. Buzug, Reference-free Ground Truth Metric for Metal Artifact Evaluation in CT, *Med Phys* **38**(7) (2011), 4321–4328.

[17] R.M. Lewitt and R.H.T. Bates, Image reconstruction from projections: IV: Projection completion methods (computational examples), *Optik* **50** (1978), 269–278.

[18] B. De Man et al., Reduction of Metal Streak Artrifacts in X-ray Computed Tomography Using a Transmission Maximum a Posteriori Algorithm, *IEEE Trans. Nuclear Science* **47** (2000), 977–981.

[19] B. De Man, J. Nuyts, P. Dupont, G. Marchal and P. Suetens, An Iterative Maximum-likelihood Polychromatic Algorithm for CT, *IEEE Transaction on Medical Imaging* **20**(10) (2010), 999–1008.

[20] E. Meyer, R. Raupach, M. Lell, B. Schmidt and M. Kachelrieb, Normalized metal artifact reduction (NMAR) in computed tomography, *Med Phys* **37** (2010), 5482–5493.

[21] A. Mouton et al., A novel intensity limiting approach to Metal Artefact Reduction in 3D CT baggage imagery, ICIP, 2012 19th IEEE International Conference on Image Processing, 2012, pp. 2057–2060.

[22] J. Müller and T.M. Buzug, Spurious structures created by interpolation-based CT metal artifact reduction, Proc. SPIE 7258 72581Y-1, 2009.

[23] J.C. Roeske, C. Lund, C.A. Pelizzari, X. Pan and A.J. Mundt, Reduction of computed tomography metal artifacts due to the Fletcher-Suit applicator in gynecology patients receiving intracavitary brachytherapy, *Brachytherapy* **2** (2003), 207–214.

[24] L. Shepp and Y. Vardi, Maximum Likelihood Reconstruction for Emission Tomography, *IEEE Trans. Medical Imaging* **1** (1982), 113–122.

[25] S. Tohnak, A.J.H. Mehnert, M. Mahoney and S. Crozier, Dental CT metal artifact reduction based on sequential substitution, *Dentomaxillofacial Ridiology* **40** (2011), 184–190.

[26] G. Wang, D.L. Snyder, J.A. Osullivan and M.W. Vannier, Iterative deblurring for CT metal artifact reduction, *IEEE Trans Med Imaging* **15** (1996), 657–664.

[27] J. Wang and L. Xing, A Binary Image Reconstruction Technique for Accurate Determination of the Shape and Location of Metal Objects in X-ray Computed Tomography, *Journal of X-ray Science and Engineering* **18**(Issue 4) (2010), 403–414.

[28] Y. Zhang et al., A New CT Metal Artifacts Reduction Algorithm Based on Fractional-order Sinogram Inpainting, *Journal of X-ray Science and Engineering* **19**(Issue 3) (2011), 373–384.

[29] S. Zhao, D.D. Robertson, G. Wang, B. Whiting and K.T. Bae, X-ray CT metal artifact reduction using wavelets: An application for imaging total hip prostheses, *IEEE Trans Med Imag* **12**(12) (2000).
[30] S. Zhao, K.T. Bae, B. Whiting and G. Wang, A wavelet method for metal artifact reduction with multiple metalic objects in the field of view, *Journal of X-ray Science and Technology* **10** (2001), 67–79.